Chapter 9

The CRRES/MEA data base and radiation belt model

The CRRES mission and its instrumentation have been described in Technical Note 4 of the TREND-2 study (Heynderickx & Lemaire 1992). A first study of the Medium Energy Analyzer (MEA) data was performed in TREND-2 (Rodgers 1996, Lemaire et al. 1995).

9.1 Introduction

The CRRES/MEA data (Vampola et al. 1992) instrument has provided information on energetic electrons throughout the inner and outer belts of the magnetosphere. Its high time resolution, good pitch angle and energy resolution and continuous data coverage has made its data extremely useful for studying the Earth's radiation environment. This chapter describes the use made of the MEA data in the TREND-3 study, i.e. the creation of a new radiation belt model.

9.2 Creation of an improved database

In the TREND-2 study (Lemaire et al. 1995), it was found that processing the MEA data from supplied data files was prohibitively time consuming. Frequent passes through the same data have to be made in performing statistical analysis and recalculating derived parameters, such as B and L, for each data point in each pass was prohibitively slow. Hence a reduced database of the available data was made with a number of new parameters added. This was very effective and the compact database was used in a study of different coordinate systems for use in radiation belt modelling. The MEA data analysis in the TREND-2 study was principally concerned with the outer belt. However, it was realised in that study, that the data could be used to study the inner belt too.

There were a number of reasons why the database produced in TREND-2 was not good enough for use in the TREND-3 study:

- Foldover: no correction was made for the depressed count rates in the inner belt, caused by excessively high fluxes.
- Time resolution: the 5 minute time resolution was appropriate for the outer belt, when the satellite moves slowly, but led to smearing of the data and consequently high standard deviations in the inner belt.
- Pitch angle resolution: the pitch angle resolution at 10° had been found in TREND-2 to be quite coarse. This proved to be particularly important since one of the ordering parameters selected for the new model depended on the magnetic field at the mirror point and this field is a sensitive function of pitch angle.
- Data coverage: only a third of all the data were in the database.

The new database is a compromise, trying to accurately represent the data while making large reductions in its size and speeding up data processing. The entire database is 0.8 Gb and fits comfortably onto a DAT tape or two magneto-optical disk sides. It is about 10 times larger than the TREND-2 database.

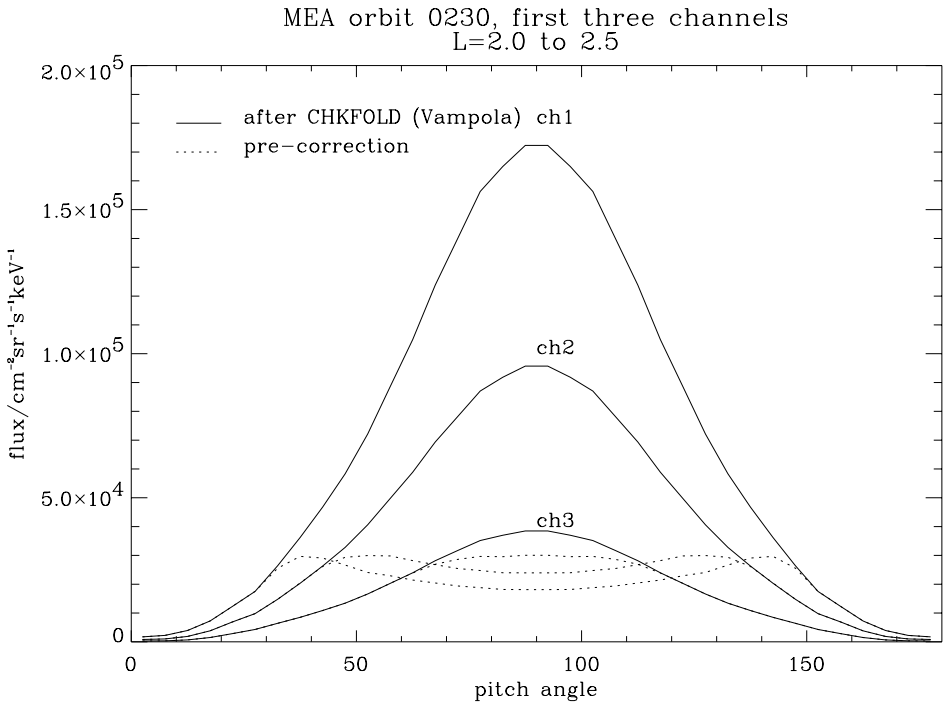

Figure 9.1. MEA Fluxes before and after the foldover correction in the three lowest energy channels, plotted against pitch angle

Table 9.1. Definitions of the parameters in the new MEA data base

Parameter	Data type	Array length	Content
year	INTEGER*4	1	Year (since 1900)
doy	INTEGER*4	1	Day of year at start of orbit
it	INTEGER*4	1	Minutes of day
agll	REAL*4	1	PLGD Calculation of L
aglb	REAL*4	1	PLGD Calculation of B
aglb0	REAL*4	1	PLGD Calculation of B_0
along	REAL*4	1	Longitude
alat	REAL*4	1	Latitude
aalt	REAL*4	1	Altitude (km)
ablb	REAL*4	1	BLXTRA Calculation of B
ablb0	REAL*4	1	BLXTRA Calculation of B_0
aloct	REAL*4	1	Local time
aglbm	REAL*4	18	Mirror field based on PLGD calculation
aglalpha0	REAL*4	18	Equatorial pitch angle based on PLGD calculation
ablbm	REAL*4	18	Mirror field based on BLXTRA calculation
ablalpha0	REAL*4	18	Equatorial pitch angle based on BLXTRA calculation
abllm	REAL*4	18	BLXTRA Calculation of L
aflux	REAL*4	18,18	Flux as function of pitch angle and energy

9.2.1 Vampola's foldover correction

The MEA was fully calibrated on the ground but it appears that count rates in space were higher than expected. As with all counting instruments, dead-time effects become significant when count rates are high. Usually this effect is taken out by the calibration. However, above a critical count rate further counts lead to a decrease in measured counts. This can only be inferred because it causes a dip in pitch angle near 90° when a peak is expected. It is a problem only for the lowest four energy bins because fluxes in the higher energy bins are never too high. In the TREND-2 study, this problem was avoided by considering chiefly the outer radiation belt where fluxes at all energies remain below the critical threshold.

In this study, we have made use of a correction algorithm provided by Vampola. This makes the assumption that the ratio of fluxes at two energies at a certain pitch angle when flux levels are below the threshold for counts saturation is a good approximation of the same ratio when flux levels exceed this threshold.

While the flux is below the critical value (about 45,000 counts per 0.512 s sample period), continuous monitoring takes place of the flux ratio between the bottom 5 energy bins. These ratios are stored as a list. If flux in one of these bins exceeds the critical value, then the data

are assumed suspect in that bin and in the ones of lower energy. Using the lowest energy with flux below the critical flux, the fluxes are propagated down to lower energy, using the latest list of ratios. It is clear that over extended periods of foldover the actual pitch angle fluxes could change but this effect is likely to be small compared to the foldover itself. Figure 9.1 compares corrected and uncorrected fluxes for four energies during a typical inner radiation belt measurement. The foldover correction clearly has a large effect on the data.

9.2.2 Changes to resolution and format

The time resolution was set to 1 minute. This makes the maximum change in L over the binning period, near perigee, about 0.1 R_{E}. The date was added to each data record. Previously it had to be inferred from the orbit number which formed part of the file name. The pitch angle, which previously had values from 0° to 180° in 10° increments, now takes values from 0° to 90° in 5° increments. Hence, the new pitch angle resolution is higher but we have lost the ability to distinguish whether particles are travelling up or down a field line. The new data format is defined by the following Fortran statement:

```
 write (outunit)
&  year, doy, it, agll, aglb, aglb0, along, alat, aalt,
&  ablb, ablb0, aloct, aglbm, aglalpha0, ablbm, ablalpha0,
&  abllm, aflux
```

The definitions of the parameters are given in Table 9.1.

9.3 Data analysis

9.3.1 Characteristics of the radiation belts

Because it covers the radiation belts in terms of energy, L and pitch angle, CRRES/MEA data can provide a comprehensive overview of this region. Figure 9.2 shows equatorially mirroring fluxes as a function of L for four different K_{p} ranges at 153 keV. At these low energies, fluxes are highest in the inner belt. The effect of increasing K_{p} is a small decrease in inner radiation belt fluxes and a large increase in outer radiation belt fluxes. At higher energies (as shown in Fig. 9.3), there is an increase in flux in both inner and outer belts. The most striking effect is the filling of the slot region.

9.3.2 Time lag correlation analysis

Correlation analysis was used in TREND-2 on Meteosat-3 and GOES-7 data. We have extended this analysis to the CRRES/MEA data. However, because CRRES is not geostationary and has full angular resolution, more comparisons can be made. The interpretation is more difficult,

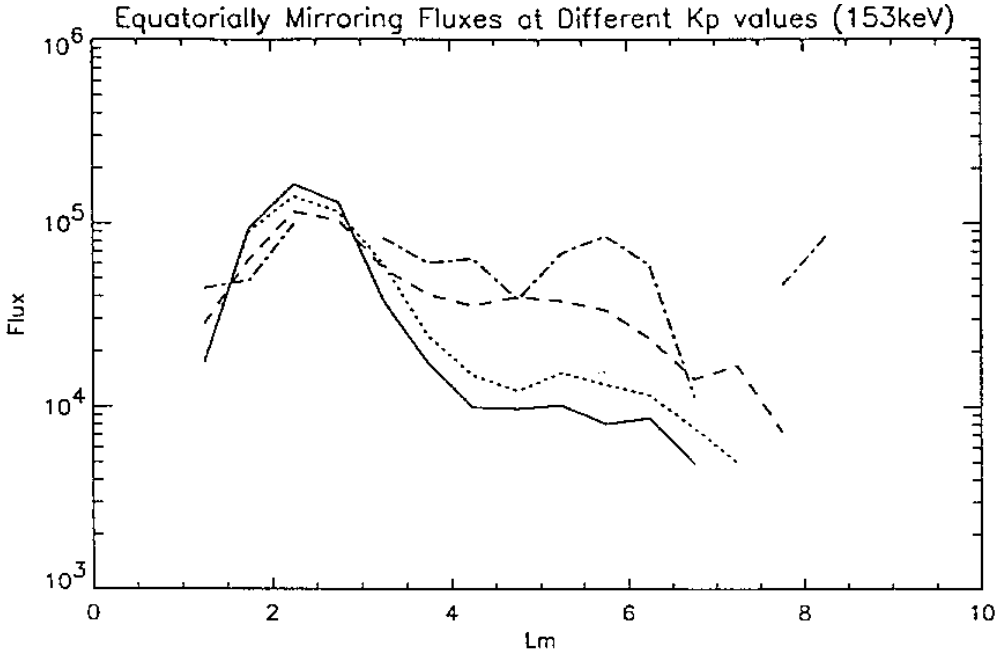

Figure 9.2. Equatorially mirroring flux as a function of L at 153 keV. Solid line: $K_{\rm p} \leq 1$, dotted line: $1 < K_{\rm p} \leq 3$, dashed line: $3 < K_{\rm p} \leq 5$, dash-dotted line: $5 < K_{\rm p} \leq 7$.

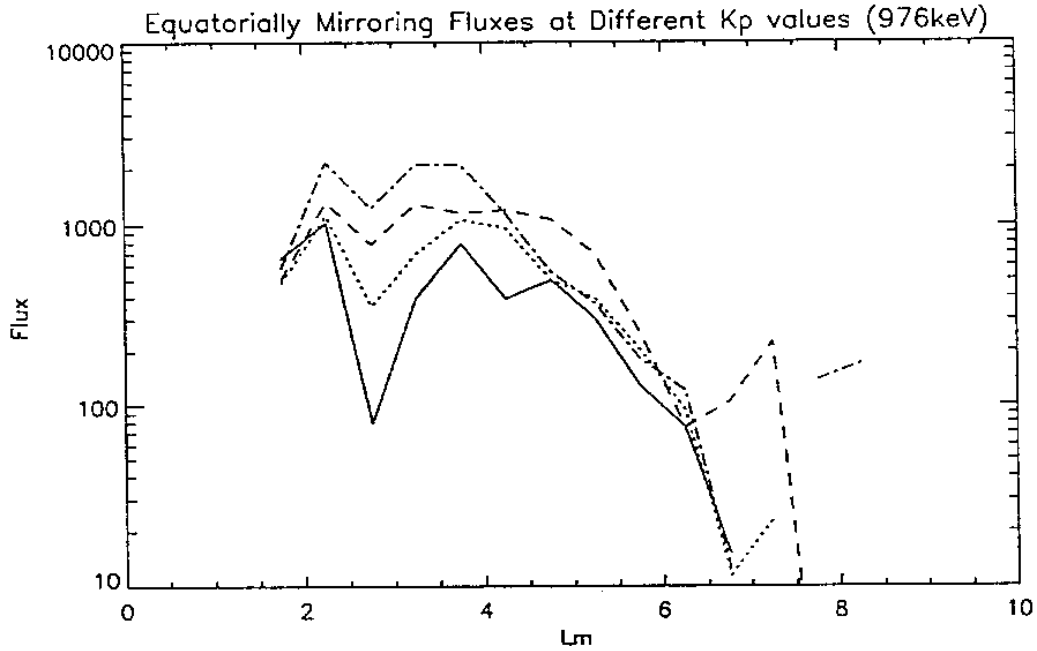

Figure 9.3. Equatorially mirroring flux as a function of L at 976 keV. Solid line: $K_{\rm p} \leq 1$, dotted line: $1 < K_{\rm p} \leq 3$, dashed line: $3 < K_{\rm p} \leq 5$, dash-dotted line: $5 < K_{\rm p} \leq 7$.

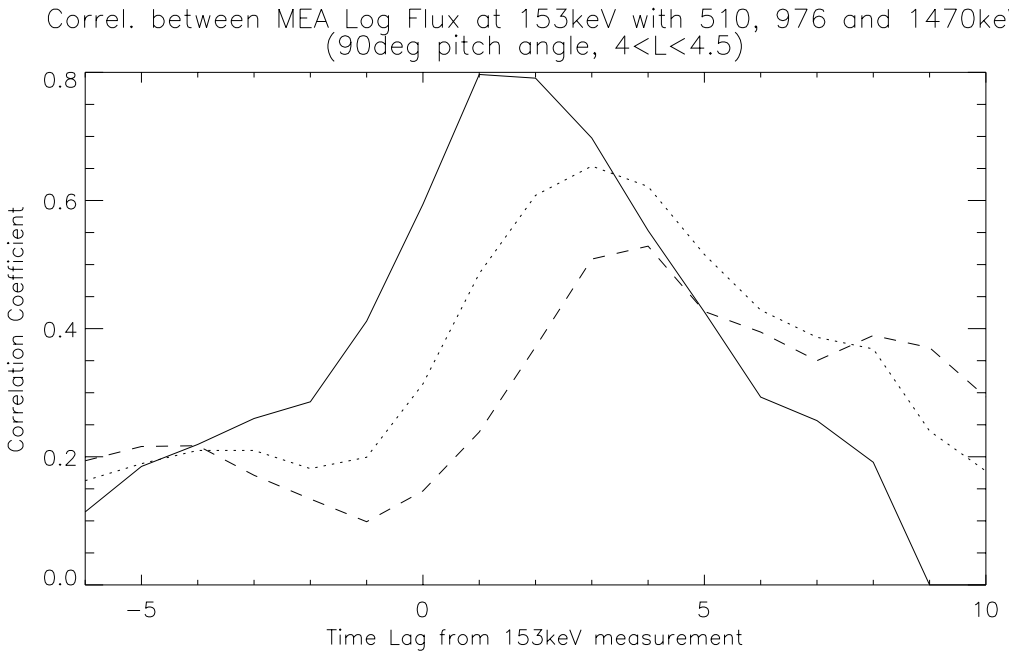

Figure 9.4. Time delayed correlation coefficients for fluxes at $L = 4.0$–4.5 comparing 153 keV and 510 keV (solid line), 153 keV and 976 keV (dotted line), and 153 keV and 1470 keV (dashed line)

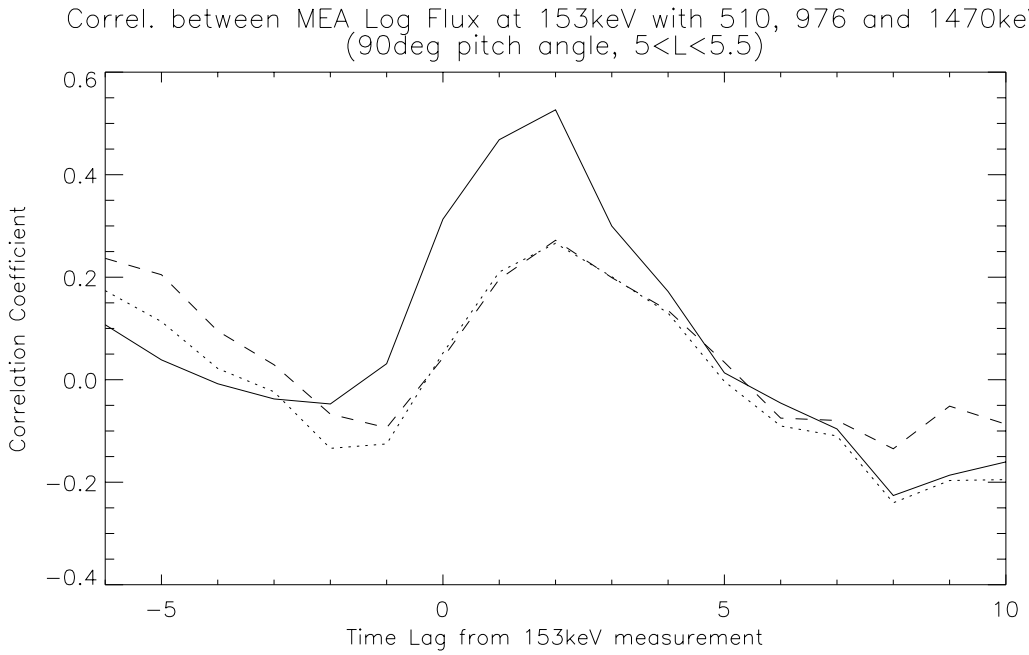

Figure 9.5. Time delayed correlation coefficients for fluxes at $L = 5.0$–5.5 comparing 153 keV and 510 keV (solid line), 153 keV and 976 keV (dotted line), and 153 keV and 1470 keV (dashed line)

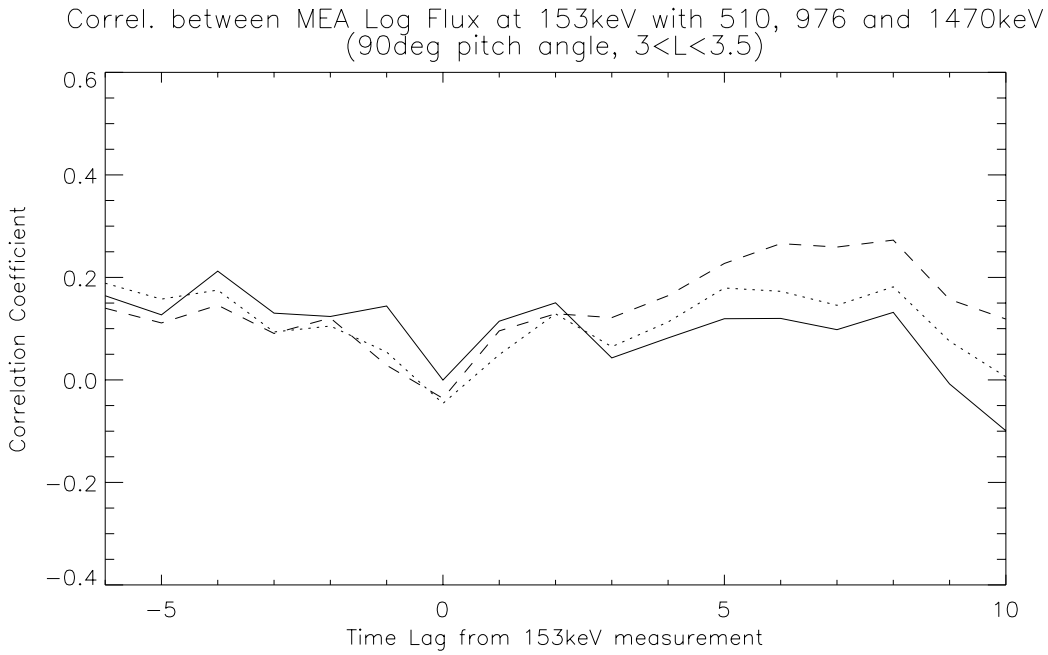

Figure 9.6. Time delayed correlation coefficients for fluxes at $L = 3.0$–3.5 comparing 153 keV and 510 keV (solid line), 153 keV and 976 keV (dotted line), and 153 keV and 1470 keV (dashed line)

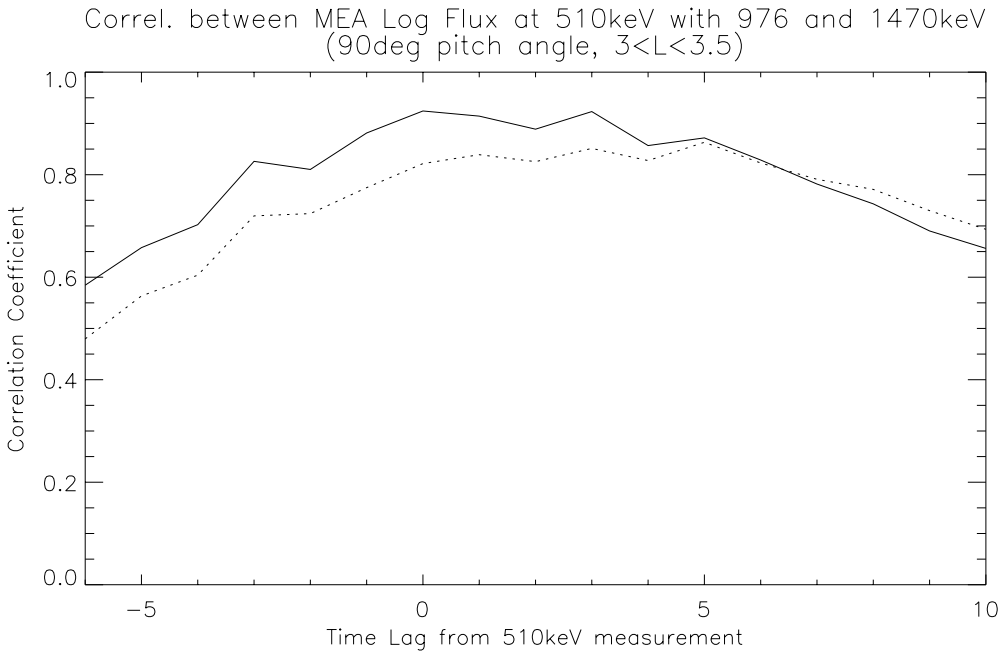

Figure 9.7. Time delayed correlation coefficients for fluxes at $L = 3.0$–3.5 comparing 510 keV and 976 keV (solid line), and 510 keV and 1470 keV (dotted line)

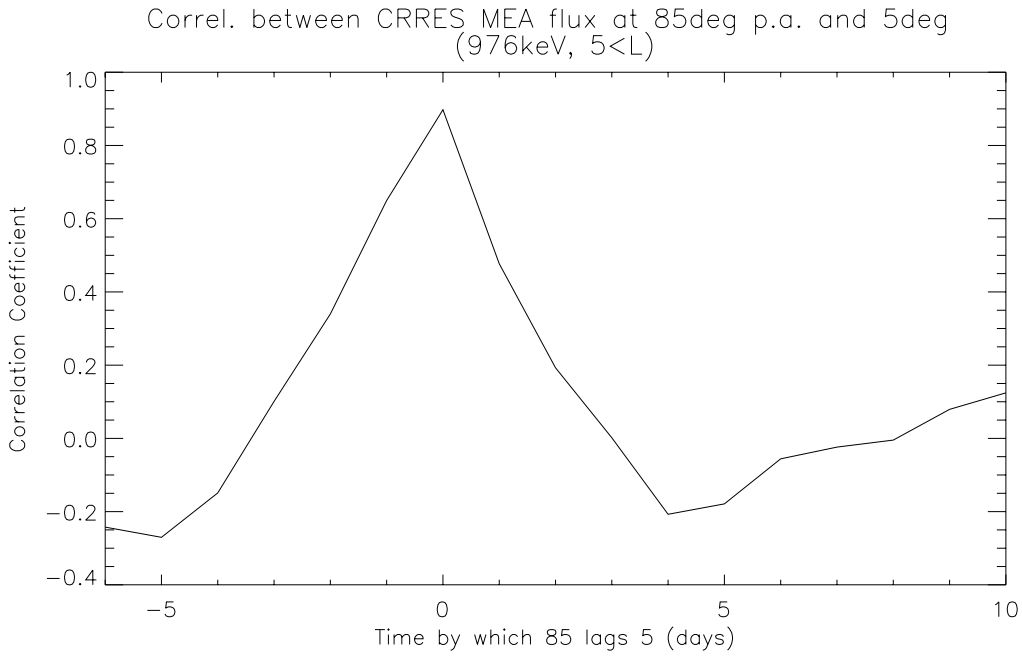

Figure 9.8. Correlation coefficient between 80°–90° fluxes and 0°–10° fluxes

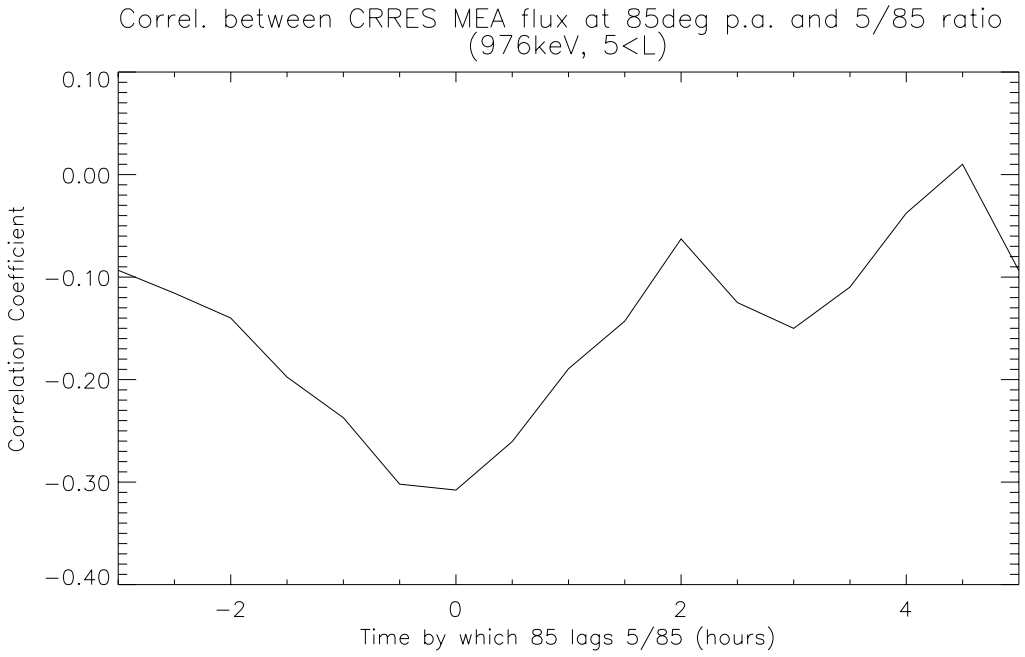

Figure 9.9. Correlation coefficient between 80°–90° fluxes and the ratio of fluxes at 0°–10° and 80°–90°

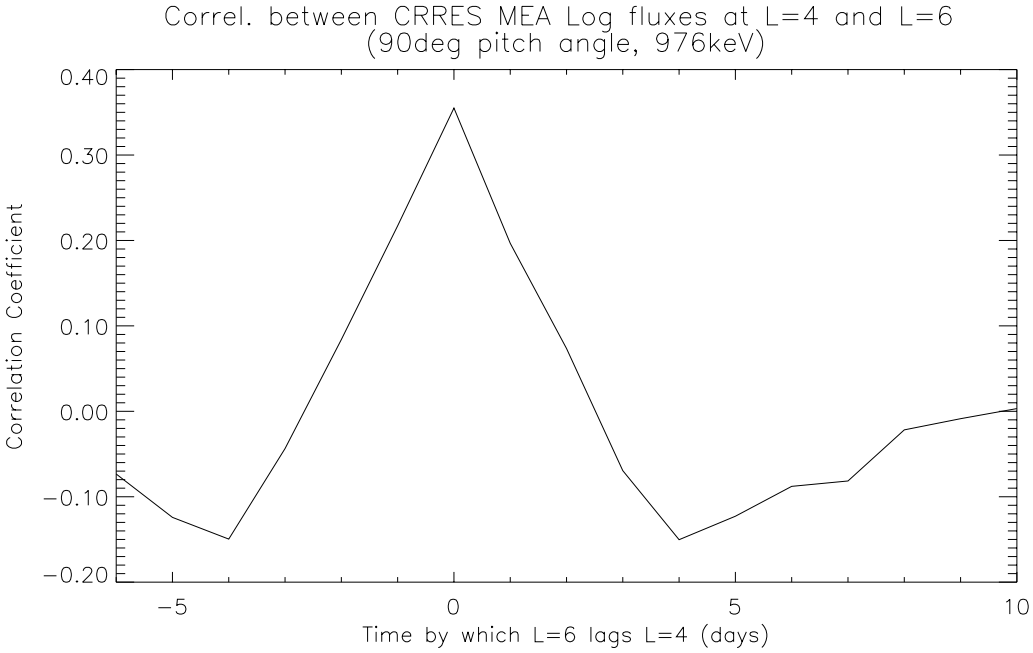

Figure 9.10. Correlation coefficient between 976 keV, 80°–90° fluxes at $L = 4$ and $L = 6$

however, because the flux observed by CRRES is continuously varying because of its orbital motion. By comparing fluxes at different energies, L values, and pitch angles, it is possible to tell the sequence of flux rises in the radiation belts. These can be used to support theories of the creation of the radiation belts, but the absence of expected correlations may just mean that other variations are more sigificant. For instance, it is possible that the magnetosphere undergoes compression and expansion which result in adiabatic heating and cooling as well as L and pitch angle changes but which return the radiation belts to their original state. Such events may swamp out source events. The use of log fluxes in this analysis prevents the results being dominated by just the highest flux events.

9.3.2.1 Energy correlation

Figure 9.4 shows the correlation coefficient achieved by comparing fluxes at 153 keV and 510 keV in the outer radiation belt between $L = 4.0$ and $L = 4.5$. This shows that higher energy fluxes are associated with the lower energy fluxes after a time delay of about 1.5 days. Comparing 976 keV and 153 keV gives a time delay of 3 days. For 1470 keV and 153 keV the delay is almost 5 days. This result confirms observations from Meteosat-3 and GOES at geostationary orbit and is in broad agreement with the predictions of the recirculation process.

The $L = 4.0$–4.5 band was initially studied because it covered the centre of the outer radiation belt. However, the results obtained in other L ranges were not the same and were harder to fit into the recirculation picture. Between $L = 5.0$ and 5.5, there was a 2-day delay between 153 keV and 510 keV fluxes but no further lag between 510 keV and higher energies (see

Fig. 9.5).

Between $L = 3.0$ and 3.5, comparing 153 keV with energies 510 keV and over produced only low correlation levels (see Fig. 9.6), indicating that there was little correlation between the datasets. In the same L range there was a high correlation between flux at energies 510 keV to 1470 keV (Fig. 9.7). However, the peak was very broad. This indicates that these energies rise and fall together in a characteristic period which is too long for a short lag to be observed.

9.3.2.2 Pitch angle correlation

We have examined the correlation between field-aligned and perpendicular fluxes. Such a study could in principle distinguish between an internal plasma source (such as the recirculation process) and an external source (such as the entry of Jovian electrons from the interplanetary medium). In recirculation, energized particles enter the outer magnetosphere at small pitch angles and then isotropize. In the Jovian process, electrons enter at high L values and pitch angle diffuse to lower L. This would result in flux increases occurring first at 90° and then at lower pitch angle.

The cross-correlation analysis, using daily averages is plotted in Fig. 9.8. This shows that the peak correlation coefficient occurred at zero days time lag. This implies that if there is a time delay between pitch angles it is significantly smaller than 1 day. Williams et al. (1968) observed that fluxes at > 300 keV took under 2 hours to isotropize after becoming pancaked. We are looking for diffusion in the opposite direction, nevertheless the same sort of processes are responsible. Williams et al. (1968) inferred, however, that at higher radiation belt energies diffusion should take considerably longer. Going to higher time resolution is very difficult because of the motion of the spacecraft through the magnetosphere. Figure 9.9 shows the correlation coefficient between flux in the 80°–90° bin with the ratio of fluxes at 0°–10° and 80°–90°. Taking this ratio removes the effect on the 0°–10° fluxes of the change due to the spacecraft's progression in its orbit. Data from $L > 5$ was chosen so that the spacecraft velocity was slower in order to minimize orbital effects on the total flux. The correlation coefficient was negative at zero time lag as one would expect. However, no significant positive correlation was observed at any time lag.

The reason for this result appears to be that the fluxes at 5° and 85° pitch angles are very strongly correlated and the 5°/85° ratio is very nearly constant. The comparison of the varying flux with this constant yields a low correlation. Hence there is no evidence of strong pitch angle differences on this time scale.

9.3.2.3 L Correlation

Another prediction of recirculation is that flux increases in a particular energy range should be seen first at low L values and later at higher ones. Figure 9.10 shows the correlation coefficient between fluxes at $L = 4$ and $L = 6$. It appears that the time delay between flux rises and falls at these different positions is much less than 1 day. In general, it appears that the outer radiation belt fluxes at 1 MeV rise as one. However, when comparing outer radiation belt fluxes

Table 9.2. A_{p15} Ranges used for the new MEA model

Range no.	A_{p15} Range
0	5.0–7.5
1	7.5–10.0
2	10.0–12.5
3	12.5–15.0
4	15.0–20.0
5	20.0–25.0
6	25.0–35.0
7	35.0–55.0

with fluxes in the inner belt or the slot, there is no period with significantly higher correlation coefficient than another.

9.4 An A_{p15} dependent electron model based on MEA data

Brautigam et al. (1992) described a quasi-static model of the outer electron belt. In this model, electron fluxes from the HEEF instrument were summed into L bins and it was assumed that fluxes could be treated as isotropic. The authors justified this assumption by showing that fluxes in the ranges 45°–65° and 65°–90° did not deviate far from equality. It should be noted however, that this test avoided the loss cone by a wide margin. They also paid no apparent regard to B/B_0 or an equivalent parameter to describe the distance of the measurement from the magnetic equator. The satellite spent much of its time near the magnetic equator but there will inevitably be a reduction in the accuracy of the model by ignoring variation along a field line.

The magnetic activity was represented by a 15-day summation of A_{p}. It had been found that this average, delayed by 1 day, correlated well with observed fluxes. This averaged, delayed index was named A_{p15}. Eight different values of A_{p15} were used to create an activity dependent model. In this study, the A_{p15} index was recreated using A_{p} data obtained from the NSSDC OMNI database. MEA Data from a subset of the new data base were binned in L and the same 8 A_{p15} ranges (listed in Table 9.2) as the PLGD model.

There were no data in our data subset that fell into the lowest A_{p15} range. Flux profiles for all 17 energy levels were obtained. Figure 9.11 shows results for the seven occupied A_{p15} ranges at 510 keV. At low A_{p15} there is a deep slot region. As activity increases, the slot fills in and flux in the outer belt rises as was observed in Sect. 9.3.1.

The flux at 1470 keV is represented in Fig. 9.12. This plot is comparable with the lowest energy channel of Brautigam et al. (1992), 1.55 MeV, whose data are plotted in Fig. 5 of their

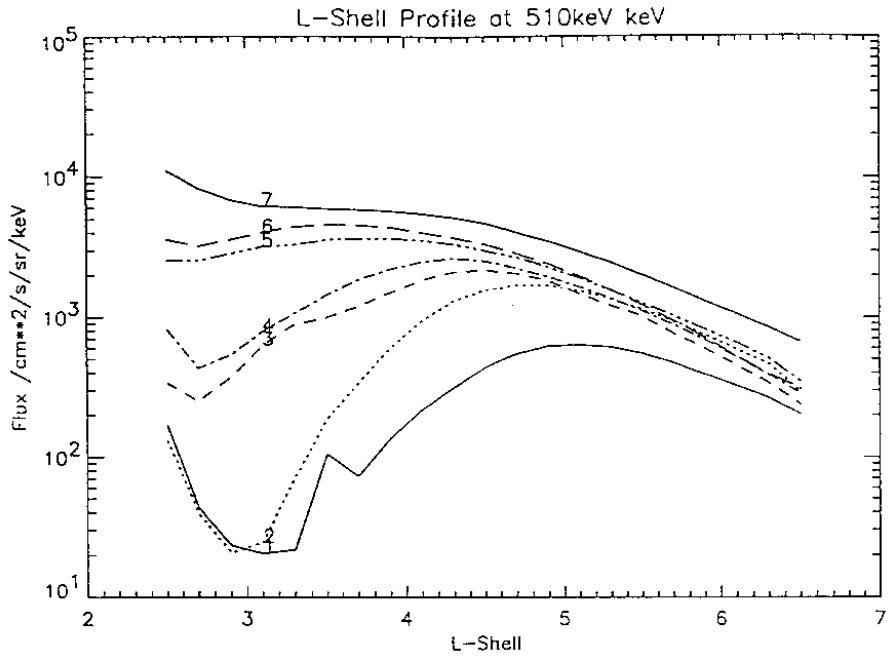

Figure 9.11. 510 keV Flux versus L for 7 ranges of A_{p15}. The zeroth range had no data and is not plotted; range 1: solid line, 2: line, 3: dashed line, 4: dot-dashed, 5: dash-triple-dotted, 6: long dashed, 8: solid.

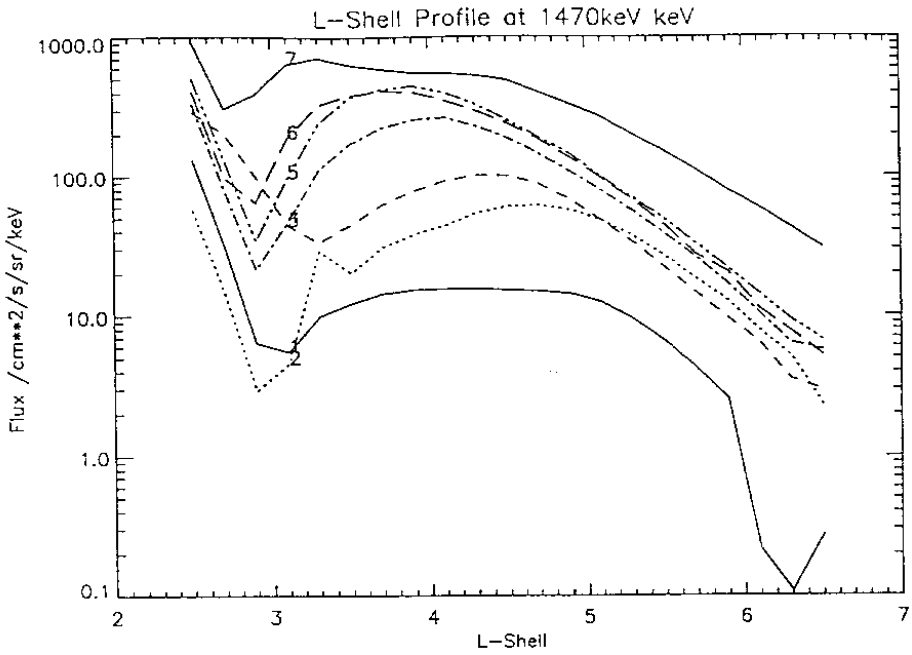

Figure 9.12. 1470 keV Flux versus L for 7 ranges of A_{p15}. The zeroth range had no data and is not plotted; range 1: solid line, 2: line, 3: dashed line, 4: dot-dashed, 5: dash-triple-dotted, 6: long dashed, 8: solid.

paper. As was noted there, when activity increases, flux increases and peaks at lower L. There is good agreement between the position and height of the peaks between the MEA data and the PLGD model. Compared to the lower energies, the filling in of the slot is more gradual but the increase in outer belt fluxes is stronger.

9.5 The ECM97 model

Based on the results of the TREND-2 study, the (L, α_0) coordinates were chosen for a new radiation belt model because this:

1. produced a high degree of systematic organization in the fluxes;
2. had reasonably low standard deviation in the outer zone;
3. was easy to visualize;
4. did not exaggerate the pitch angle resolution of the data near the loss cone;
5. and achieved adequate coverage of both inner and outer belts without changing bin sizes between the two zones.

The Tsyganenko (1989) $K_{\rm p}$ dependent external magnetic field model was used along with an internal DGRF model field. The BLXTRA software (Heynderickx et al. 1996d) was used to access the field models and calculate B and L. Separate flux maps in this coordinate system were created for each energy.

9.5.1 Statistical variation

In processing the flux map, the average fluxes were found, along with the standard deviation. Because it was based on the new database, with higher time resolution and corrected fluxes at low altitudes, the new model was expected to be valid in the inner radiation belts. The improved time and pitch angle resolution was expected also to lead to improved performance in the outer belt.

As in TREND-2, we used the standard deviation when $K_{\rm p} \leq 1$ as a measure of how well the coordinate system organizes the data because at these times natural flux variations are expected to be low. A lower ratio of standard deviation to mean is evidence that similar flux values are summed in the same (L, α_0) bins. Figure 9.13 shows the standard deviation ($K_{\rm p} \leq 1$) for the TREND-2 data at 510 keV and Fig. 9.14 shows the standard deviation at the same energy for the current study. In order to make a comparison possible, the same α_0 and L bin sizes as the TREND-2 model have been used and the TREND-3 standard deviations have been divided by $\sqrt{5}$ to account for the 5 times higher time resolution. The new data displays a number of improvements over the TREND-2 data. Unlike the earlier data base, the new one has low standard deviation throughout the outer belt. Low standard deviation has been extended across

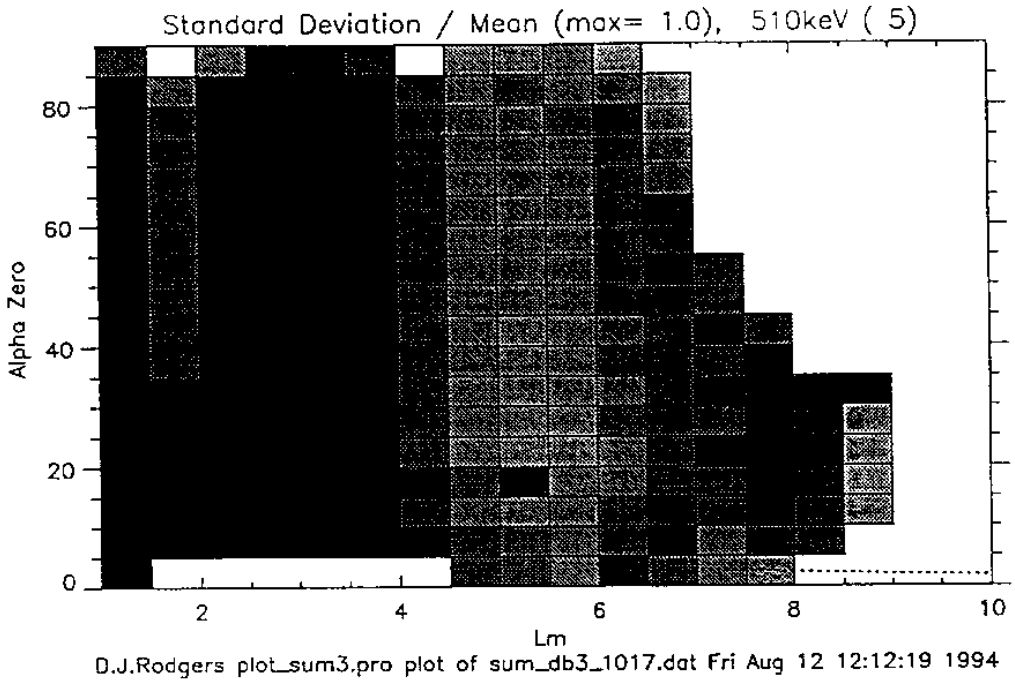

Figure 9.13. Greyscale plot of 510 keV standard deviation binned in (L, α_0) space. The dotted line represents the loss cone. Data from the TREND-2 data base were used.

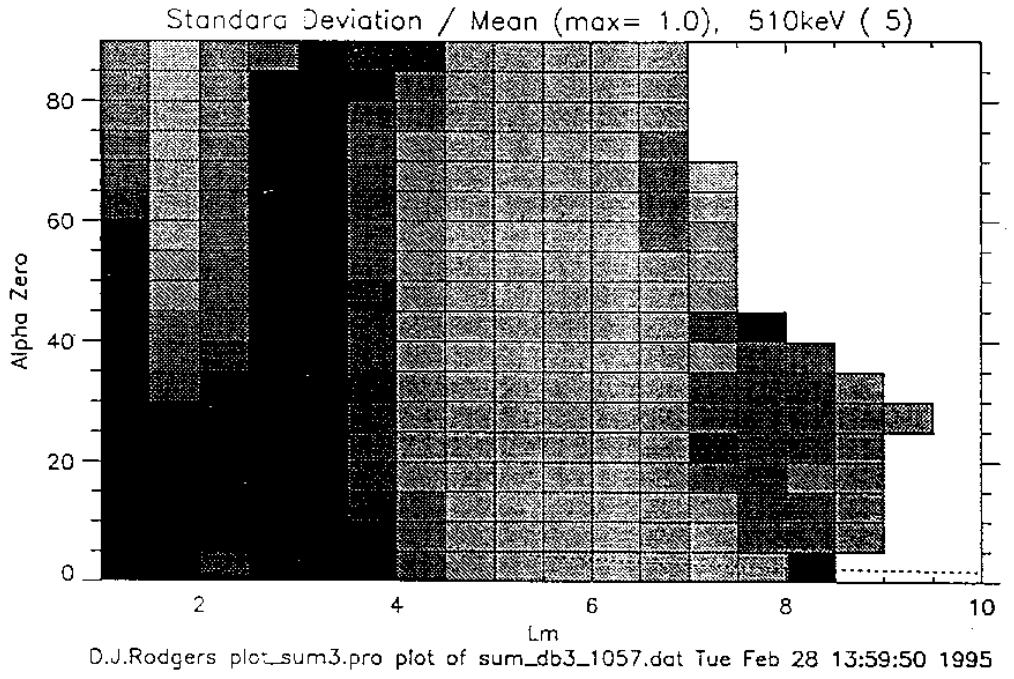

Figure 9.14. Greyscale plot of 510 keV standard deviation binned in (L, α_0) space. The dotted line represents the loss cone. Data from the TREND-3 data base were used.

almost the entire inner belt. However, standard deviations remain high in the slot region and in the loss cone. This is not unexpected since these regions have low fluxes and are highly variable. Hence, the combination of the new data base and the (L, α_0) coordinate system can create a model that is useful in both the outer and inner belts.

At low energies, in the outer belt, the standard deviation is affected by the efficiency of the binning system and by natural variations in the plasma. At higher energy and in the inner belt, the subtracted background dominates the statistics to varying degrees, depending on energy. Hence a comprehensive energy dependent variance model to complement the model of mean fluxes is not possible.

9.5.2 Contamination

Figure 9.20 shows fluxes at 976 keV. There is some flux measured in the loss cone in the inner and outer belts. Since fluxes were expected to be almost non-existent in this region, it was initially thought that this might represent residual noise that was not removed by MEA's on-board noise rejection.

An investigation was carried out into these loss-cone fluxes. Figure 9.15 shows equatorially field aligned flux versus L in four energy ranges. At all energies there are significant fluxes. If contamination from penetrating radiation were the cause, then the flux in each energy should correspond to the same count rate in the raw data, since the size of the each anode is about the same. Back-calculating the counts from the flux results in the counts shown in Fig. 9.16. Because it is not possible to reverse the effect of the foldover correction, the values in the inner belt are not correct. In the outer belt it is clear that there is not a constant count rate at each energy. This makes contamination unlikely to be the cause.

Further evidence for this is given by a comparison between loss cone fluxes and energetic protons, the most probable source of any contamination. Figure 9.17 shows the time variation of 976 keV flux over a period of 2 months at $L = 4$. Figure 9.18 shows the 3 MeV proton flux over the same period, using data taken from the CRRES Science Summary Data Base. There is no similarity. Figure 9.19 shows the 1 MeV electron data from the same database. This shows the behaviour of all electrons, not just those in the loss cone. The similarity to the loss cone flux is very strong, indicating that the loss cone flux rises and falls along with the rest of the electrons. Hence, contamination is not responsible in this case.

The loss cone in the outer belt is only 6° at $L = 4.5$, the heart of the outer belt. Inaccuracies in pitch angle measurements could have the effect of moving electrons apparently into the loss cone. However, this explanation does not work for the inner belts, where the loss cone is around 20°.

9.5.3 (L, α_0) Binning

To create the new model, flux maps were created by binning data from approximately 900 CRRES orbits with L resolution 0.2, an improvement in resolution from the model created in

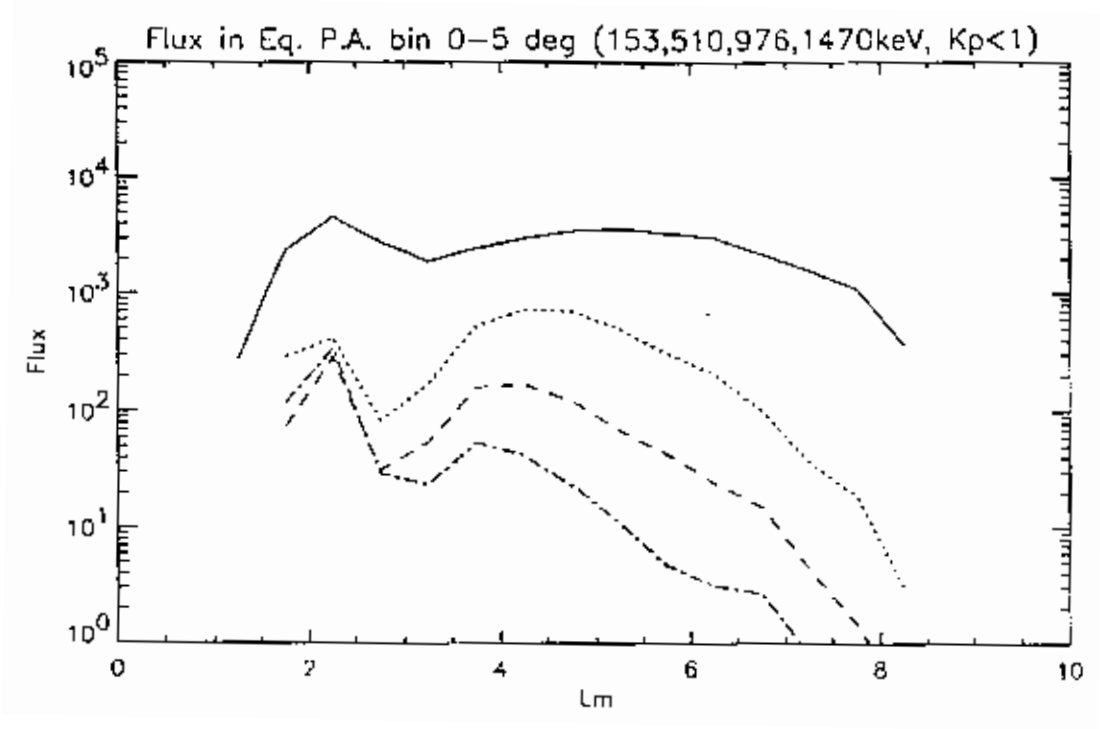

Figure 9.15. Fluxes in 0°–10° equatorial pitch angle bin for energies 153, 510, 976 and 1470 keV

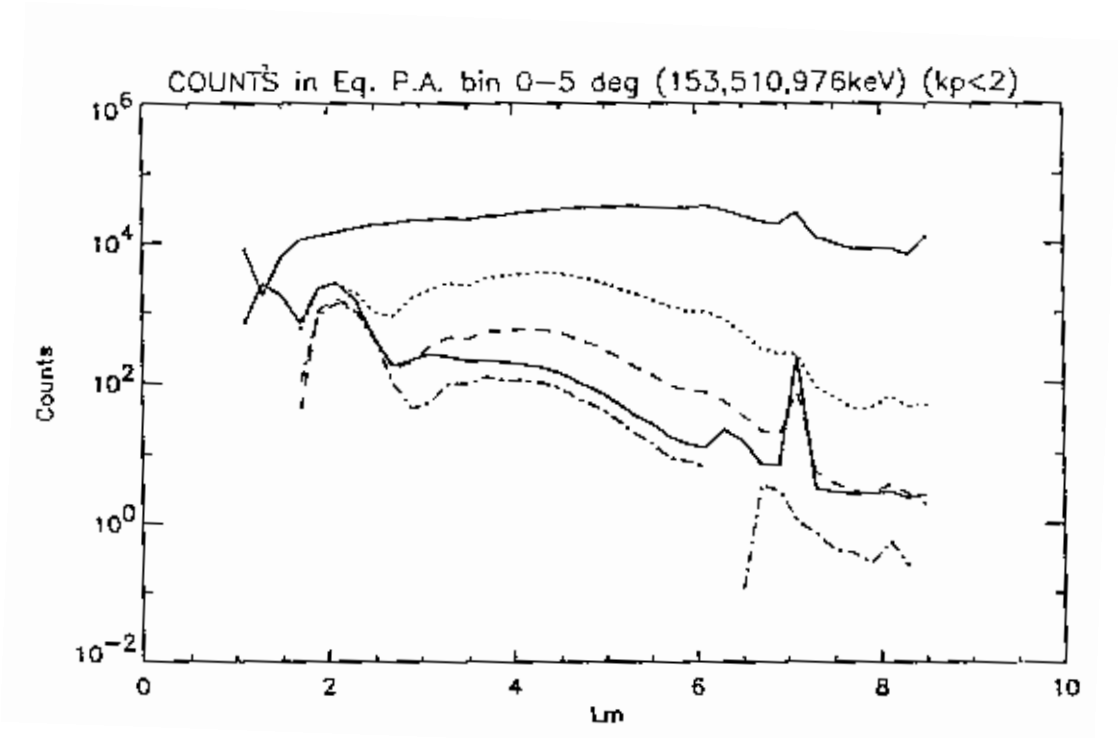

Figure 9.16. Back-calculated counts in 0°–10° equatorial pitch angle bin for energies 153, 510, 976 and 1470 keV. The background channel is shown by a thicker solid line.

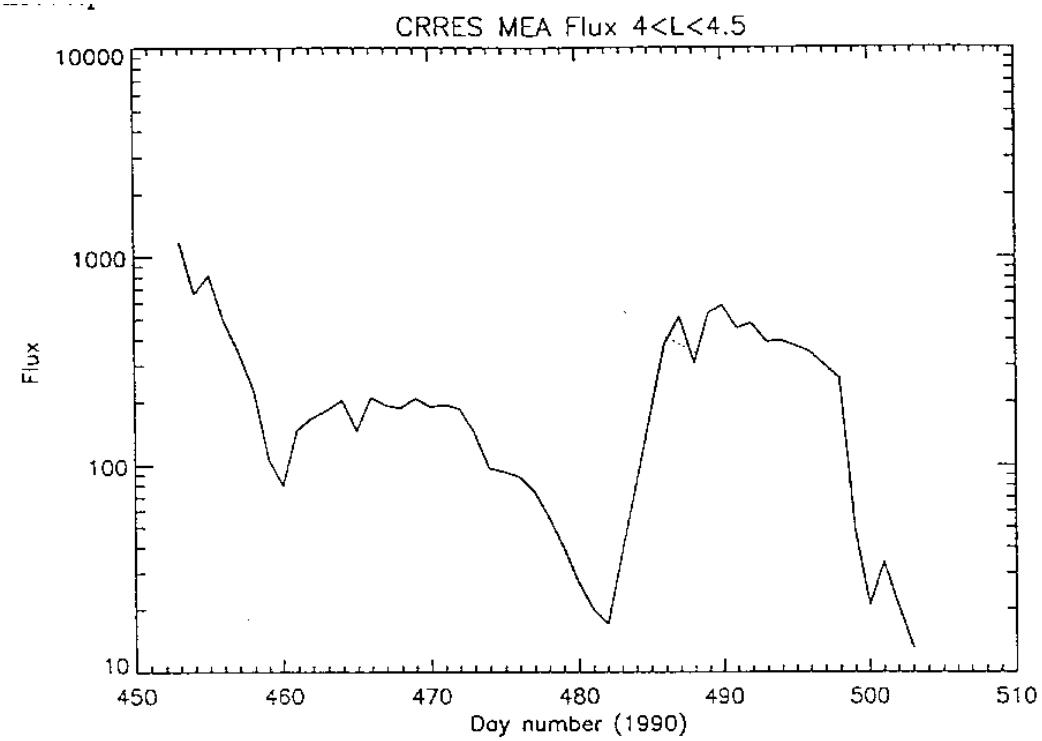

Figure 9.17. Loss-cone fluxes at $L = 4$ over a 2-month period

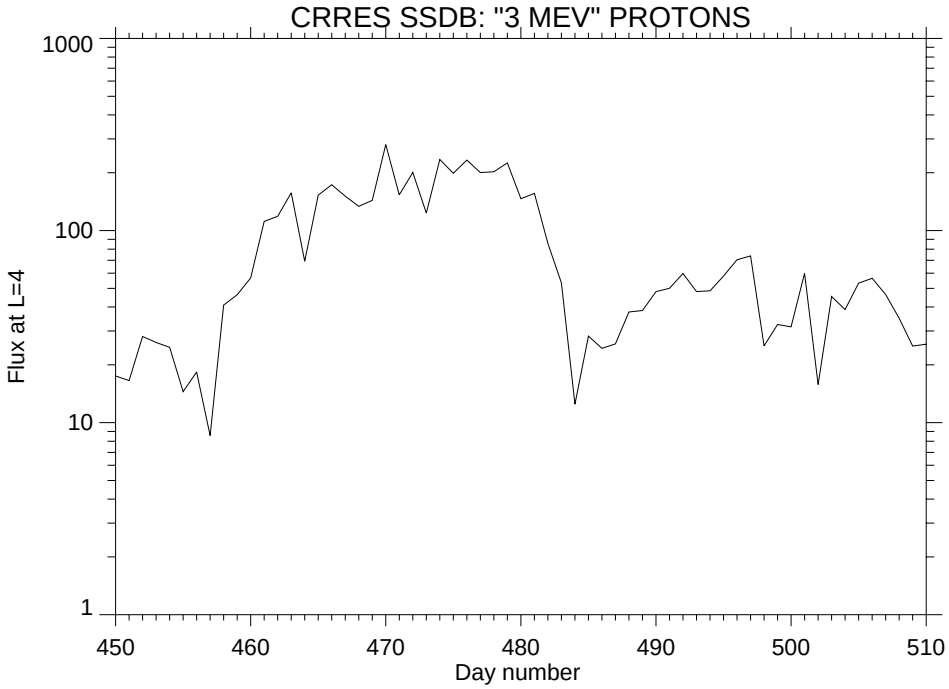

Figure 9.18. 3 MeV Proton flux over the same 2-month period as in Fig. 9.17

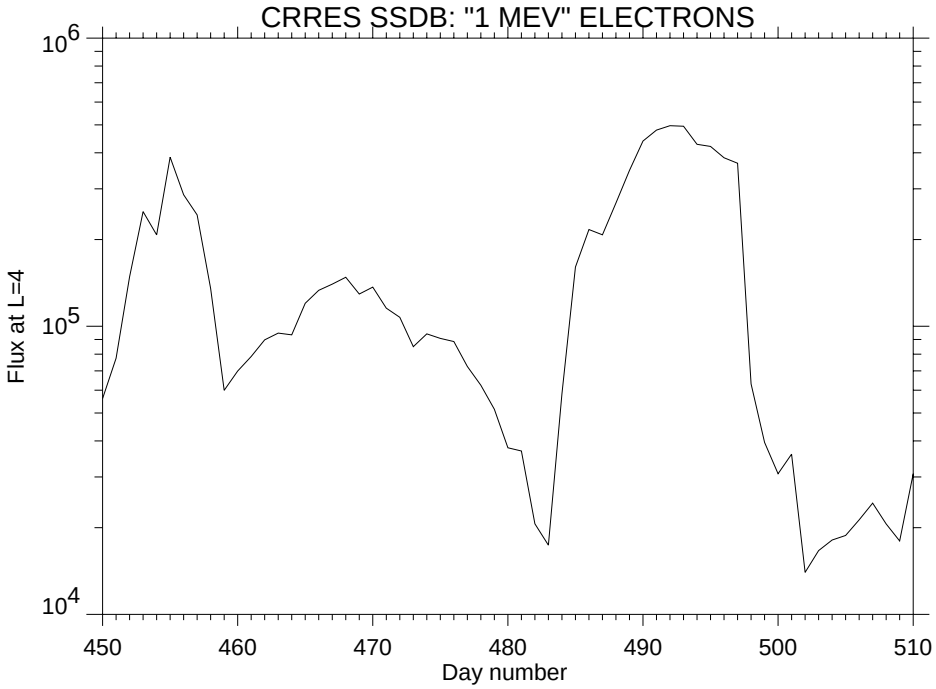

Figure 9.19. Total 1 MeV electron flux over the same 2-month period as in Fig. 9.17

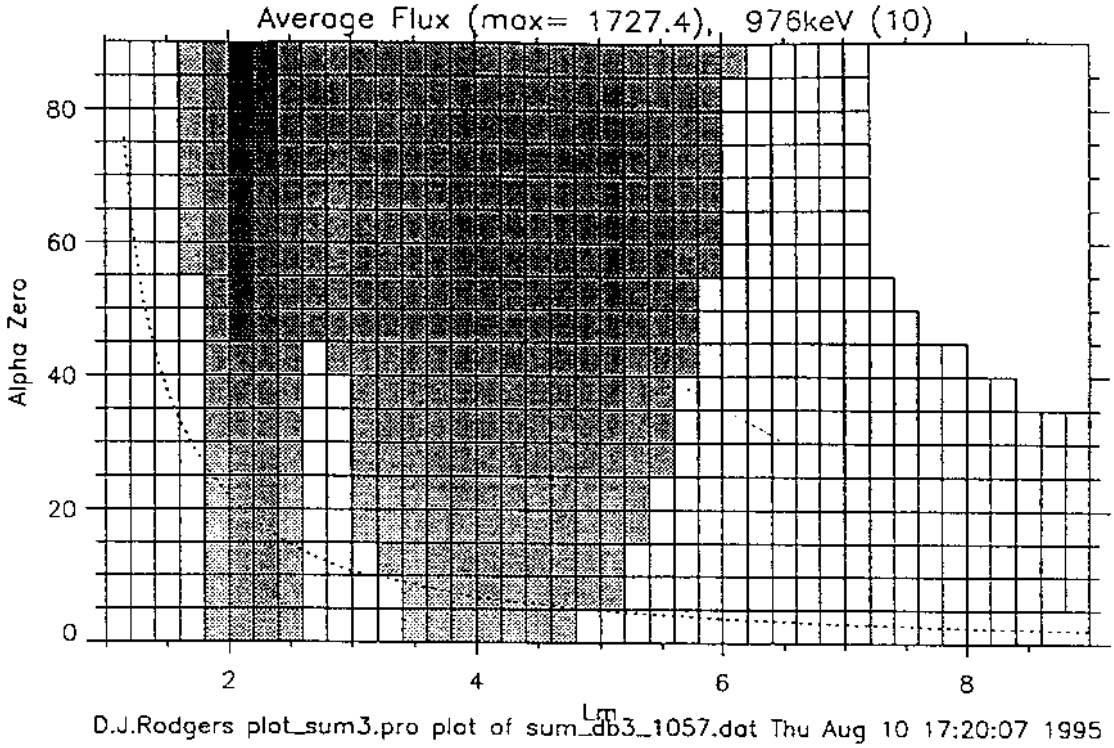

Figure 9.20. Greyscale plot of 976 keV mean flux binned in (L, α_0) space. The dotted line represents the loss cone.

TREND-2. The pitch angle resolution was 5° as in the TREND-2 work but here the raw data were summed to that accuracy, instead of 10° as in TREND-2. Finer binning in pitch angle is not justified because of the limited instrument pitch-angle resolution. The model ranges from $L = 1$ to $L = 9$, from $\alpha_0 = 0°$ to $\alpha_0 = 90°$, and from 153 keV to 1534 keV. An example of the resulting flux map is shown in Fig. 9.20 for 976 keV electrons.

9.5.4 Model Format

Five versions of the model were created, one each for the K_p ranges 0 to 1^+, 2 to 3^+, 4 to 5^+, and 6 to 7^+, and one for all K_p values combined. The corresponding flux maps have been converted to the format described in Sect. 2.1.6 and added to TREP. The combined model is called ECM97.

9.5.5 Comparison with AE-8

Figure 9.21 shows a flux profile at local noon along the sunward equator at 1 MeV for NASA's AE-8 model (Vette 1991a) and the ECM97 model. The peak flux in the two models is similar but the MEA model drops off faster with radius. This difference becomes more pronounced in the tailward direction (Fig. 9.22). The AE-8 model predicts almost no difference from the sunward fluxes but ECM97 drops more rapidly with radius. The difference around geostationary orbit is an order of magnitude. Part of this difference is due to the presence of an external component to the magnetic field model used with the ECM97 model, and part is due to the fact that AE-8 does not take into account pitch angle dependence when constructing omnidirectional fluxes.

9.5.6 Model Characteristics

Figure 9.23 shows contours of log flux in a noon-midnight slice through the magnetosphere for K_p=0 at 500 keV. The sampling grid has a resolution of 0.5 R_E. The inner and outer belts are clearly visible. The sunward and tailward sides are fairly symmetric.

Figure 9.24 shows contours of log flux for the same slice as in Fig. 9.23 with K_p=7. The tailward side of the magnetosphere is now severely compressed, an effect of using a realistic magnetic field model. The peak of the outer belt has moved earthwards and the slot has disappeared. There are some irregularities at the edges of the model due to the poorer statistics for high $K_\mathrm{p}$values. Overall flux levels in the inner and outer belt are much higher than for low K_p.

9.5.7 Outstanding problems

The model is presently contaminated by high energy protons for energies above 500 keV up to $L = 3$. Hence, its use is currently restricted to the outer belt.

In the outer belt the loss cone has a width of only a few degrees, which means that the MEA angular resolution does not characterise it accurately. This has no effect on fluxes near the

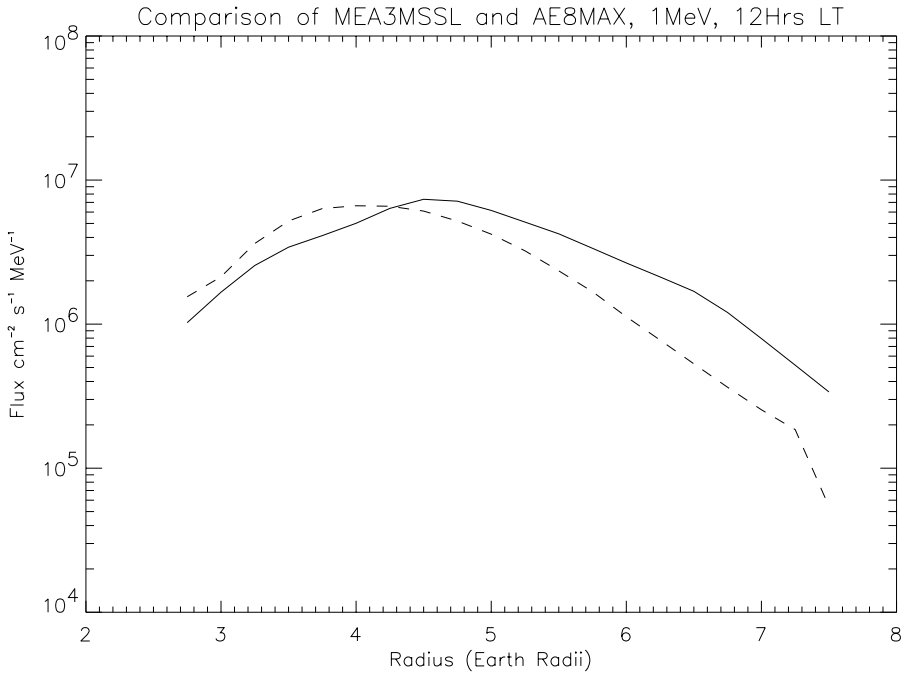

Figure 9.21. 1 MeV Electron flux along the noon equator. The solid line is AE-8 MAX and the dotted line is ECM97.

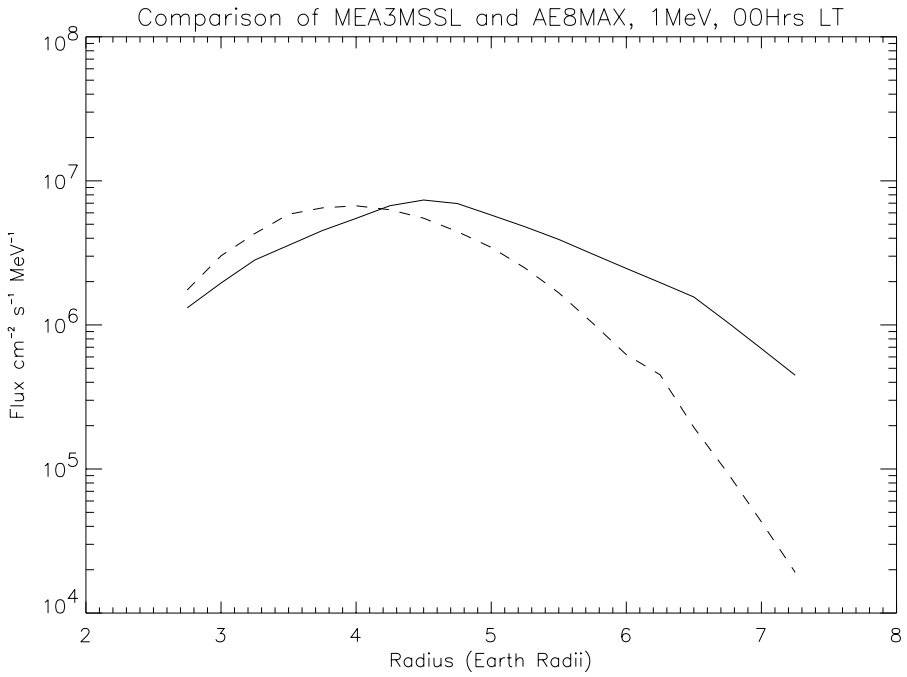

Figure 9.22. 1 MeV Electron flux along the midnight equator. The solid line is AE-8 MAX and the dotted line is ECM97.

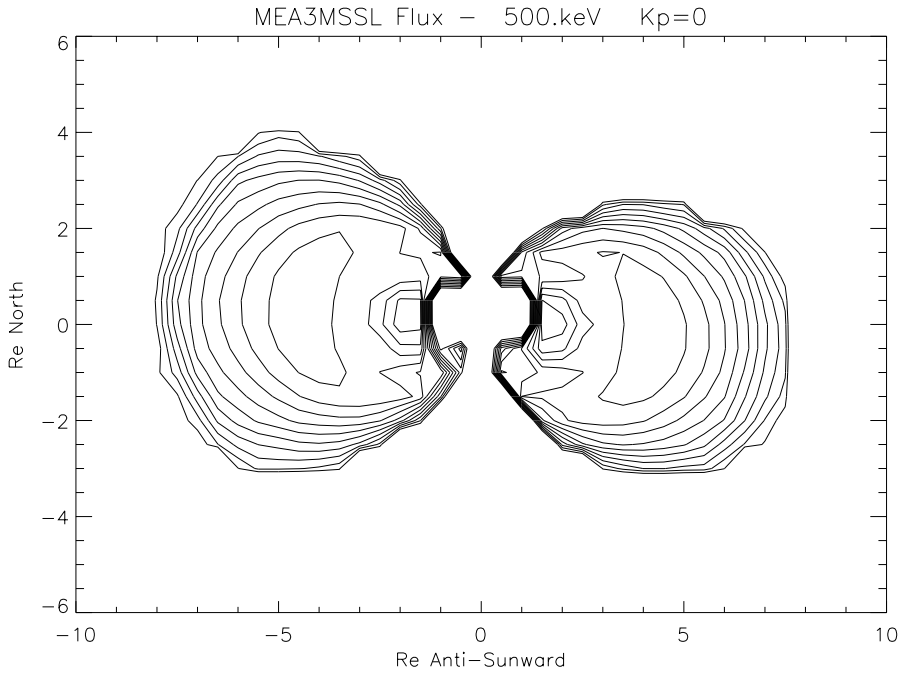

Figure 9.23. Contour plot of log flux in a noon-midnight cut through the magnetosphere, for $K_{\rm p} = 0$. The sunward direction is to the left.

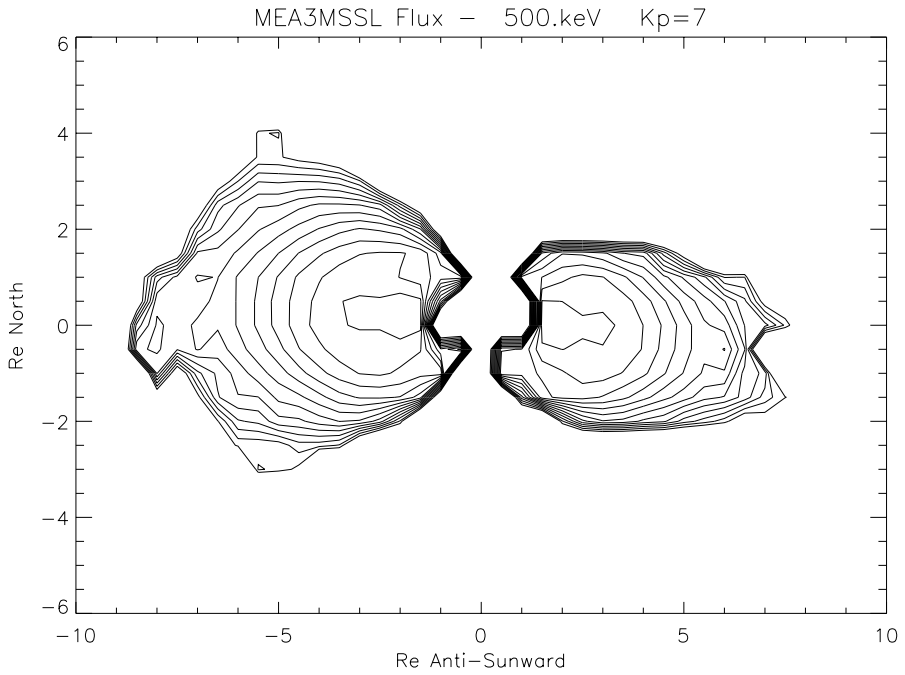

Figure 9.24. Contour plot of log flux in a noon-midnight cut through the magnetosphere, for $K_{\rm p} = 7$. The sunward direction is to the left.

equator but results in the model becoming less accurate at low altitudes. This contrasts strongly with AE-8 which mapped the loss cone carefully.

The sudden change in the inner belt fluxes that occurred in March 1991 have shown that the 18 month CRRES mission is not a long enough data base to average out infrequent large events.

9.6 Feasibility of a statistical model

One of the most useful aspects of the Meteosat analysis in TREND-2 was the demonstration of how the variation of fluxes was reduced as the time bin over which the measurements were averaged was increased. The result was a model of flux variance as a function of time duration. The Meteosat analysis began with 30 minute averages and progressively increased the time bin up to a year. This worked because Meteosat covered a small L range and fluxes at the lower energies did not have a steep gradient in L. For CRRES, this is far more difficult because of its wide coverage in L and the steep gradient of fluxes at higher energies. Figure 9.25 shows the distribution of fluxes summed over 1 minute, for 976 keV electrons at $L = 6.6 \pm 0.25$. The mode of the flux is the lowest flux bin of 0–1 $\mathrm{cm}^{-2}\mathrm{sr}^{-1}\mathrm{keV}^{-1}$. When the data were averaged over 2 and 4 minutes, there was no perceptible difference.

However, when the time bin was 8 minutes as shown in Fig. 9.26, the peak at low fluxes has considerably decreased compared with the high flux tail. In this plot, the vertical scale is an eighth of that in Fig. 9.25 to keep the data directly comparable. The total number of data points in Fig. 9.26 is less than 8 times fewer than in Fig. 9.25 because few data periods are available with 8 minutes coverage at this L value, even though the spacecraft is near apogee. Extending this analysis to longer time bins is not possible. It should also be noted that much of the variation in fluxes in short time bins comes from L dependent variation. Hence, a model such as was created with Meteosat is not practical until data are summed over multiples of orbits.

Only a third of orbits had any data in the L range specified. Figure 9.27 shows a histogram of fluxes binned in one complete orbit. From this plot the mean and 10^{th}, 50^{th} and 90^{th} percentiles have been found. These are plotted for successive multiples of the orbital period in Fig. 9.28. As in the Meteosat-3 data all three percentiles start to converge on the mean as the binning period increases. However, poor statistics make some of them diverge again at 16 orbits and above. Hence, only on a time scale of 1–4 minutes or 1–8 orbits can a statistical model be created. This would be of limited use.

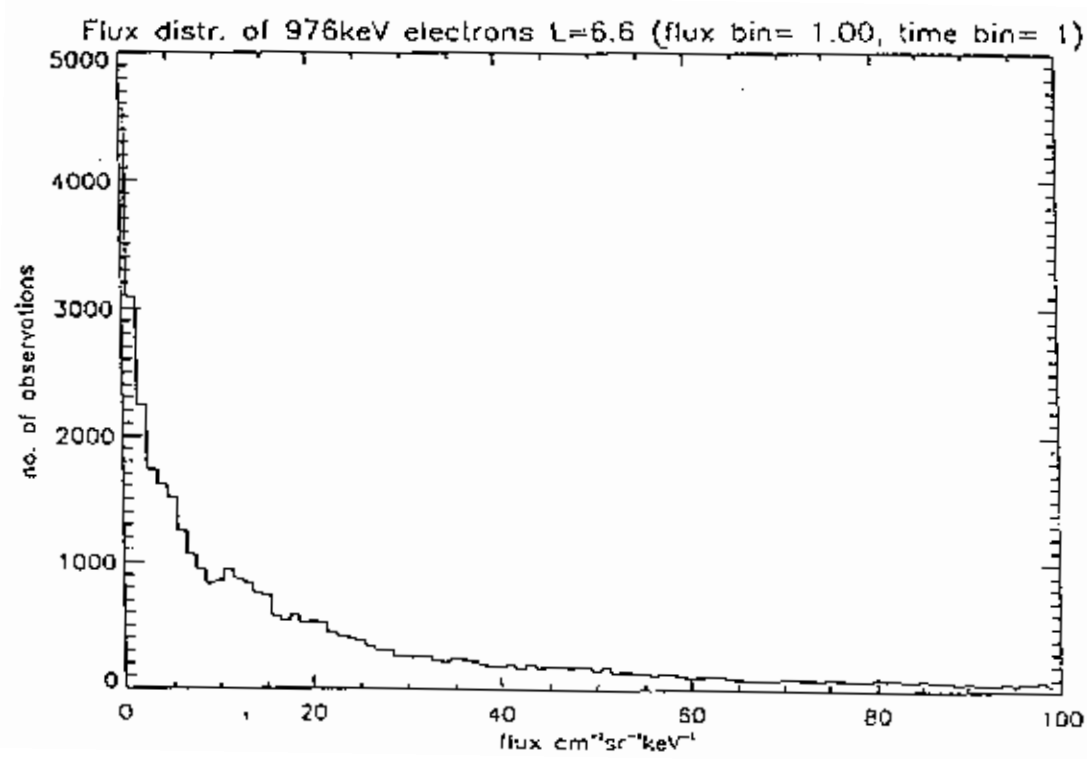

Figure 9.25. 976 keV Electron fluxes at $L = 6.5$–6.7 summed over 1 minute

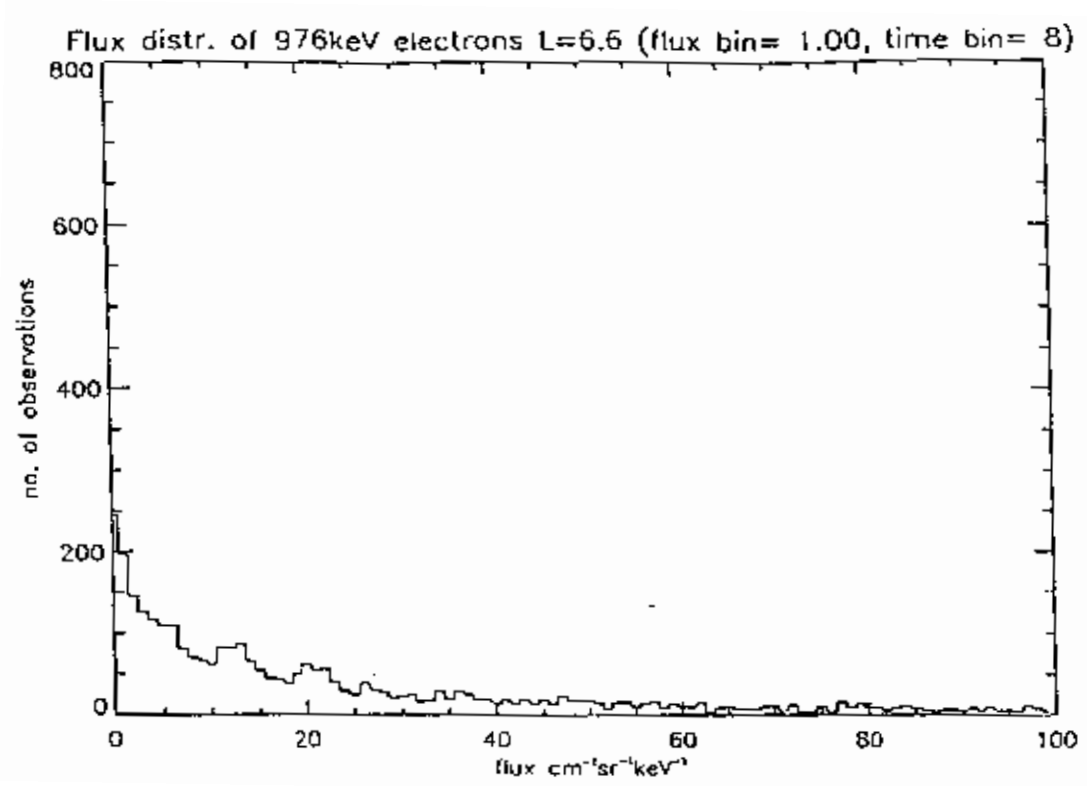

Figure 9.26. 976 keV Electron fluxes at $L = 6.5$–6.7 summed over 8 minutes

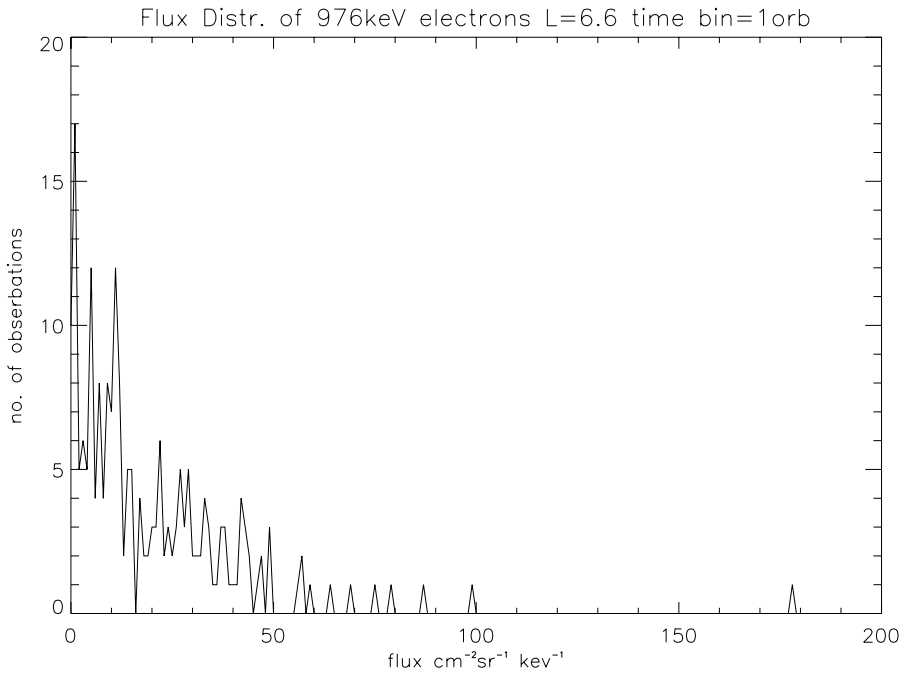

Figure 9.27. 976 keV Electron fluxes at $L = 6.5$–6.7 summed over 1 orbit

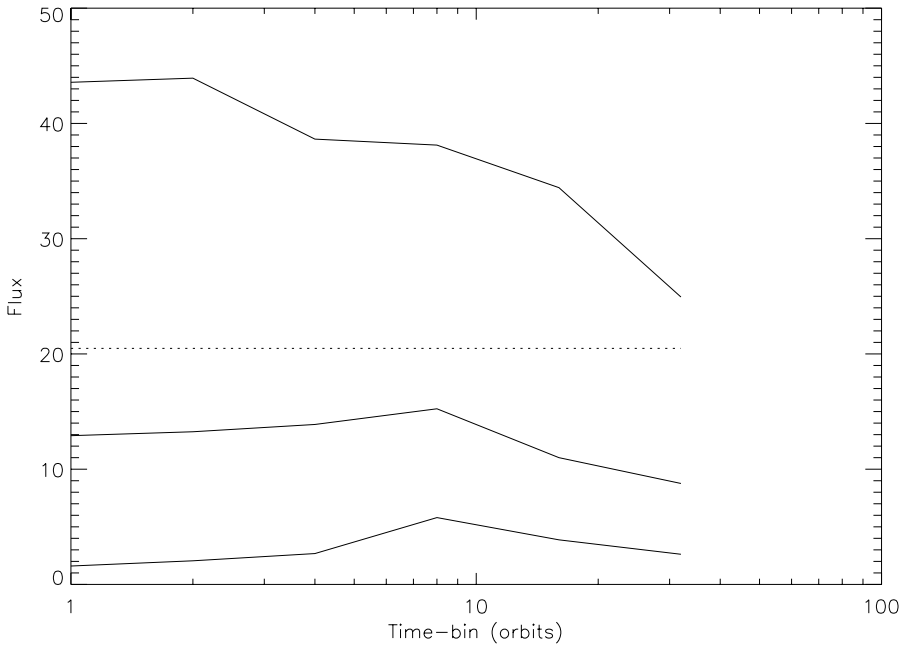

Figure 9.28. Dependence of median, and 10^{th} and 90^{th} percentiles on time bin